Mapping the ionized gas of the metal-poor HII galaxy PHL 293B with MEGARA[⋆]

C. Kehrig[1]†, J. Iglesias-Páramo[1,2], J.M.Vílchez[1], A. Gil de Paz[3,4],
S. Duarte Puertas[1], E. Pérez-Montero[1], A.I. Díaz[5], J. Gallego[3,4], E. Carrasco[6],
N. Cardiel[3,4], M. L. García-Vargas[7], A. Castillo-Morales[3,4], R. Cedazo[8],
P. Gómez-Álvarez[7], I. Martínez-Delgado[7], S. Pascual[3,4], A. Pérez-Calpena[7]

[1] *Instituto de Astrofísica de Andalucía, CSIC, Apartado de correos 3004, 18080 Granada, Spain*
[2] *Estación Experimental de Zonas Aridas (CSIC), Ctra. de Sacramento s/n, E-04120, Almer; Spain*
[3] *Departamento de Física de la Tierra y Astrofísica, Fac. CC. Físicas, Universidad Complutense de Madrid, Plaza de las Ciencias 1, E-28040 Madrid, Spain*
[4] *Instituto de Física de Partículas y del Cosmos IPARCOS, Fac.CC Físicas, Universidad Complutense de Madrid, Plaza de las Ciencias, 1, E-28040 Madrid, Spain*
[5] *Departamento de Física Teórica, Universidad Autónoma de Madrid, E-28049 Madrid, Spain*
[6] *Instituto Nacional de Astrofísica, Óptica y Electrónica, INAOE, Calle Luis Enrique Erro No.1, C.P. 72840, Tonantzintla, Puebla, Mexico*
[7] *FRACTAL, S.L.N.E., Calle Tulipán 2, portal 13, 1A, E-28231 Las Rozas de Madrid, Spain*
[8] *Universidad Politécnica de Madrid, 28031, Madrid, Spain*

ABSTRACT
Here we report the first spatially resolved spectroscopic study for the galaxy PHL 293B using the high-resolution GTC/MEGARA integral field unit (IFU). PHL 293B is a local, extremely metal-poor, high ionization galaxy. This makes PHL 293B an excellent analogue for galaxies in the early Universe. The MEGARA aperture (∼ 12.5" × 11.3") covers the entire PHL 293B main body and its far-reaching ionized gas. We created and discussed maps of all relevant emission lines, line ratios and physical-chemical properties of the ionized ISM. The narrow emission gas appears to be ionized mainly by massive stars according to the observed diagnostic line ratios, regardless of the position across the MEGARA aperture. We detected low intensity broad emission components and blueshifted absorptions in the Balmer lines (Hα,Hβ) which are located in the brightest zone of the galaxy ISM. A chemically homogeneity, across hundreds of parsecs, is observed in O/H. We take the oxygen abundance 12+log (O/H) = 7.64 ± 0.06 derived from the PHL 293B integrated spectrum as the representative metallicity for the galaxy. Our IFU data reveal for the first time that the nebular HeIIλ4686 emission from PHL 293B is spatially extended and coincident with the ionizing stellar cluster, and allow us to compute its absolute HeII ionizing photon flux. Wolf-Rayet bumps are not detected excluding therefore Wolf-Rayet stars as the main HeII excitation source. The origin of the nebular HeIIλ4686 is discussed.

Key words: HII regions — galaxies: dwarf — galaxies: individual: PHL 293B — galaxies: ISM — galaxies: starburst

1 INTRODUCTION

HII galaxies are the most metal-poor starbursts in the local Universe (e.g., Westera et al. 2004; Kehrig et al. 2006; Izotov, Thuan, & Guseva 2012; James et al. 2017). These galaxies present intense star-formation rates, and they usually have low masses and blue optical colours. The hot, luminous massive stars present in HII galaxies give off vast quantities of high-energy UV

photons which ionize the gas producing strong nebular emission-line spectra (e.g., Kehrig, Telles, & Cuisinier 2004; Cairós et al. 2009, 2010).

PHL 293B is a very compact HII galaxy (effective radius of its star-forming component ∼ 0.7"; e.g., Papaderos et al. 2008) which belongs to the "Palomar-Haro-Luyten" survey of faint galaxies (see French 1980; Kinman & Davidson 1981). The ionized gas of PHL 293B presents a very low oxygen abundance of 12+log(O/H) ≈ 7.6-7.7 [∼ 1/10 solar metallicity[1];

---

[1] assuming a solar abundance 12+log(O/H)$_\odot$ = 8.69 (Asplund et al. 2009)

e.g., French (1980); Kinman & Davidson (1981); Papaderos et al. (2008); Izotov et al. (2011); Fernández et al. (2018)]. Moreover, PHL 293B shows ultra-high excited gas indicated by the presence of the nebular HeIIλ4686 emission (e.g., French 1980; Izotov, Thuan & Guseva 2007), and its very high specific star formation rate (sSFR = SFR/$M_\star$ ~ 6 Gyr^{-1}; see table 4 from Filho, et al. 2013) is comparable to those found in the high-redshift Universe (e.g., Stark 2016). These features are more commonly observed and predicted in distant star-forming galaxies in comparison with local starbusrst (e.g., Lehnert, et al. 2015; Mainali, et al. 2018; Izotov, Thuan & Guseva 2019; Sobral, et al. 2019). This makes PHL 293B a remarkable place nearby that allows us to study in detail physical conditions which may be predominant in primeval starbursts (see also Kehrig, et al. 2016; Guseva, et al. 2017; Izotov, et al. 2018; Kehrig, et al. 2018; Senchyna, et al. 2019). The optical spectrum of PHL 293B shows the typical strong narrow emission lines normally seen in the spectra of HII galaxies. Besides, its spectrum exhibits other features as low-intensity broad wings and blueshifted narrow absorptions in the hydrogen recombination lines (e.g., Izotov & Thuan 2009; Terlevich et al. 2014, and references therein). Table 1 lists other general properties of PHL 293B. Fig. 1 shows a three-colour composite image of PHL 293B from the Hubble Space Telescope (HST)/WFC3 which reveals an extended gaseous nebulae and star-forming activity mainly present in the southern zone of the galaxy (see also Papaderos et al. 2008).

In the last years, spatially resolved spectroscopy has opened a new window onto our understanding of the ionized gas in low-redshift SF galaxies, preventing us from an over-simplified view of it (e.g., Kehrig et al. 2008, 2013; Duarte Puertas, et al. 2019; Ucci, et al. 2019; Sánchez 2020). In this work, we present the first 2D spectroscopic study of PHL 293B based on commissioning observations with the *Multi Espectrógrafo en GTC de Alta Resolución para Astronomía* (MEGARA; see next section). Our MEGARA data provide a detailed scanning of the structure and properties of the PHL 293B ionized gas. Moreover, we derive the first integrated spectrum and total HeII-ionizing photon flux from PHL 293B.

The paper is organized as follows. In Section 2, we report observations and data reduction. Flux measurements and emission line intensity maps are presented in Section 3. In Section 4 we show the 2D view of the ionization structure and nebular properties. In Section 5, we present the integrated properties from selected regions of PHL 293B. Section 6 discusses the spatially resolved HeIIλ4686-emitting region and the origin of the HeII excitation. Finally, Section 7 summarizes the main conclusions derived from this work.

2   OBSERVATIONS AND DATA REDUCTION

The data of PHL 293B were obtained with MEGARA (see Gil de Paz et al. 2018; Carrasco et al. 2018), attached to the 10.4m GTC telescope at the Roque de los Muchachos Observatory. Observations were taken during the second commissioning run in 2017 July 25th and 29th, using the Large Compact Bundle (LCB) IFU mode which provides a field of view (FOV) of 12.5×11.3 arcsec^2 (~ 1.4 kpc × 1.3 kpc at the distance of 23.1 Mpc; see Fig. 1), with a spaxel^2 diameter of 0.62 arcsec. In order to cover the main op-
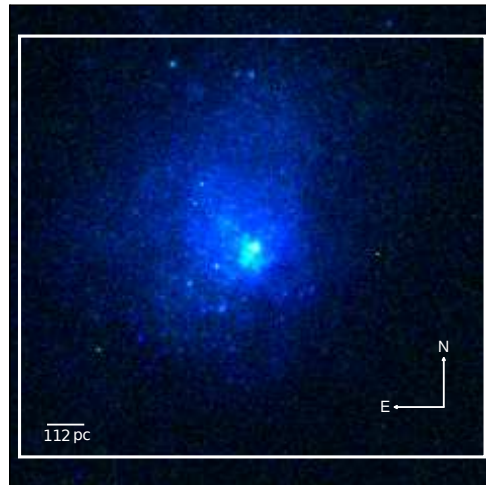

Figure 1. Colour composite HST image of PHL 293B generated using the following bands: blue = WFC3/F606W, green = WFC3/438W, red = WFC3/F814W (HST Proposal ID 12018; PI: A.Prestwich). The white box denotes the observed field of view (FOV) of MEGARA (12.5" × 11.3"). North is up and east is to the left.

Table 1. General Properties of PHL 293B

Parameter	PHL 293B
Alternate names	Kinman Dwarf, A2228-00
R.A. (J2000.0)	22h 30m 36.8s
DEC. (J2000.0)	-00° 06' 37"
redshift	0.0051
D^a(Mpc)	23.1
HType^b	Im?
Scale (pc/'')	112
(B-V)^c	0.56 ± 0.05
(V-R)^c	0.27 ± 0.04
$M_B{}^c$(mag)	-14.37
$A_V{}^d$(mag)	0.193

^{a} Distance taken from the NASA/IPAC Extragalactic Database (NED); ^{b} Hubble Type from NED; ^{c} From Cairós et al. (2001); ^{d} Galactic extinction from Schlafly & Finkbeiner (2011)

---

tical emission-lines, the observations were carried out with three gratings; we used the "blue" VPH405-LR (centered at 4025 Å) and "green" VPH480-LB (centered at 4785 Å) gratings which give spectral ranges (Å)/dispersions (Å pix^{-1}) of ~ 3653-4386/0.17 and ~ 4332-5196/0.20, respectively. On the red side, the VPH665-HR (centered at 6602 Å) was utilized, providing a spectral range from ~ 6445-6837 and 0.09 Å/pix. The resolving power of the gratings are ~ 6000 in case of LR VPHs and ~ 20000 for VPH665-HR.

We observed a total of 2.25 hours on the galaxy, with the integration time split into three exposures for each VPH: 3 × 600 s for VPH665-HR and VPH480-LR each, and 3 × 1500 s for VPH405-LR. The seeing was about 1 arcsec and 0.5 arcsec during the first and second observing nights, respectively. All science frames were observed at airmasses ≲ 1.2 to minimize the effects due to differential atmospheric refraction. Additionally, all necessary calibration frames (exposures of arc lamps and of continuum lamps) were obtained.

The data reduction and sky subtraction were carried out using the MEGARA Pipeline as described in Pascual et al. (2019). Due to severe haze throughout the observing run, we did not flux-

---

^{2} Individual elements of IFUs are usually named "spatial pixels" (so-called "spaxel"); the term is used to distinguish a spatial element on the IFU from a detector pixel.

calibrate the data using standard stars. Instead, we flux-calibrated our spectra using the Sloan Digital Sky Survey (SDSS) spectrum of PHL 293B. First, we co-added the spaxels within a 3 arcsec-diameter aperture (i.e., the same size of the SDSS fiber), centered at the brightest spaxel of the LCB IFU, to create a 1D spectrum called the "SDSS-like" MEGARA spectrum. We then measured the flux of the emission lines present in both the SDSS and SDSS-like MEGARA spectra. We compared these flux measurements by performing a third order logarithm polynomial fit to obtain the sensitivity function which was applied to the science frames. Given that the SDSS spectrum (spectral range ~ 3800-9000 Å) of PHL 293B does not cover our bluest emission lines [On]$\lambda\lambda$3727,3729Å, the sensitivity function was extrapolated to allow for their relative flux calibration.

3 FLUX MEASUREMENTS AND EMISSION LINE INTENSITY MAPS

Here we measure emission line fluxes from individual spaxels based on our own IDL scripts. On top of a linear flat continuum, we fit a Gaussian profile to each emission line using the IDL based routine MPFIT (Markwardt 2009); the peak intensity, the line width σ and the central wavelength λ_C for each line are kept as free parameters. Note that, due to the high spectral resolution of MEGARA we were able to resolve the [OII] doublet and, consequently, measure its individual lines at λ3726 Å and λ3729 Å. In the case of the Hα+[NII] lines, we perform a simultaneous fit keeping a nitrogen [NII]λ6584/[NII]λ6548 line ratio of 3. Previous work, based on single-aperture/long-slit spectroscopy of the central star-forming (SF) knot of PHL 293B, have detected the presence of several components for the Hα, Hβ lines (e.g., Izotov & Thuan 2009; Terlevich et al. 2014; Fernández et al. 2018). Following these authors, we fit these Balmer lines assuming three Gaussian components: narrow + broad emission, and one absorption component. Errors in the derived parameters (line flux, peak intensity, line width σ, central wavelength λ_C) are estimated by using the boot-strap method.

By combining the line fluxes with the position of the spaxels on the sky, we create all maps presented in this paper. Figure 2 exposes the intensity maps for several emission lines; only fluxes with S/N > 3 are displayed.[3] We show for the first time the spatial distribution for the broad Hα,Hβ components for PHL 293B. The global spatial structure of the brightest lines (narrow Hβ, [OIII]λ5007, and narrow Hα) is similar, with [OIII]λ5007 and narrow Hα emission covering almost the entire FOV. The spatial distribution of the fainter lines (e.g., [OIII]λ4363, HeIIλ4686, [NII]λ6584, [SII]λ6717+6731), and the broad Hβ and Hα are restricted to the inner parts of the galaxy.

When comparing the [OII] emission distribution to that for other relatively bright lines as Hβ, we find the former to be more compact. This could be related partially to the fact that the [OII] lines lie at the blue edge of the spectra (i.e. λ < 3750 Å) where we not only observe lower S/N but also expect less accuracy of the flux calibration (see Section 2 for details; see e.g., Sánchez, et al. 2012; Yan, et al. 2016; López-Sanjuan, et al. 2019). However, we highlight that the PHL 293B ionization structure which seems to be dominated by high excitation should also plays an important role;

e.g., the [OIII]λ5007 emission is spatially wide-ranging as long as the [OII]$\lambda\lambda$3726,3729, [NII]λ6584 and [SII]$\lambda\lambda$6717,6731 lines extend over a much smaller area (see Fig. 2). The likeness between the maps of [OII], [NII] and [SII] is generally expected due to their similar ionization potential, albeit [NII] and [SII] lines sit at the red part of the spectra where S/N and flux calibration effects mentioned above should be minor.

The emission of both, the high and low intensity lines, are peaked on the southern HII region where the star formation is mostly concentrated (the bright blue knot in Fig. 1; see also Papaderos et al. 2008). In agreement with previous work (e.g., Izotov & Thuan 2009; Terlevich et al. 2014) we were able to detect Hβ and Hα P Cygni-like profiles in some integrated spectra (see Section 5 for details) and in a few individual spaxels which are indicated in the map of the Hβ and Hα broad emission components (see Fig. 2). P Cygni-like profiles are displayed in Figs. 3 and 4.

4 SPATIALLY RESOLVED PROPERTIES OF THE IONIZED GAS

4.1 Ionization Structure

Baldwin-Phillips-Terlevich (BPT) diagrams (Baldwin, Phillips, & Terlevich 1981) are a powerful tool, widely used to separate star-forming galaxies and AGN. The spatially-resolved BPT diagrams for PHL 293B are shown in Fig. 5: [OIII]λ5007/Hβ vs. [NII]λ6584/Hα, [SII]$\lambda\lambda$6717,6731/Hα. These line ratios are not corrected for extinction, but reddening effects must be minor since these ratios involve lines which are close in wavelength. Each circle plotted in Fig. 5 corresponds to a line ratio obtained from a single spaxel, where the red circles show the HeIIλ4686-emitting spaxels. Based on stellar population synthesis and photoionization models, Kewley et al. (2001) proposed a theoretical demarcation curve that isolates galaxies with line ratios which are due to excitation by massive stars within HII regions from those where other ionizing source is needed. An empirical curve that differentiates between AGNs and HII-like systems was later derived by Kauffmann et al. (2003); both demarcation lines are plotted in Fig. 5. For all positions in PHL 293B our emission-line ratios fall in the general locus of SF objects, i.e., below and to the left of the separation lines in the two BPT diagrams. This suggests that photoionization from hot massive stars appears to be the dominant excitation mechanism within PHL 293B.

The spatial distribution for the BPT line ratios are displayed in Fig 6. While highest and lowest values of [OIII]λ5007/Hβ are found at the most inner and external zones of PHL 293B respectively, a reverse trend is observed in the [NII]λ6584/Hα and [SII]$\lambda\lambda$6717,6731/Hα maps, indicating the presence of higher excited gas inward. The [OIII]λ5007/Hβ map clearly shows larger values spatially coincident with the southern HII region (i.e., the bright blue knot in Fig. 1) which also comprises the HeII zone (see also the HeIIλ4686 map in Fig. 2). Additionally, in Fig. 5 we see that the HeII-emitting spaxels tend to have higher [OIII]λ5007/Hβ ratio in comparison to the other spaxels. Shall we note that despite this correlation, the hard HeII-ionizing radiation (E $\gtrsim$ 4 Ryd) does not have to be necessarily the main responsible for the brighter [OIII] emission since the the [OIII] lines can be excited by softer energies (E $\gtrsim$ 2.5 Ryd) (see e.g., Thuan & Izotov 2005).

---

[3] Here the S/N is defined as the ratio between the peak intensity of the emission line and the standard deviation of its underlying continnum.

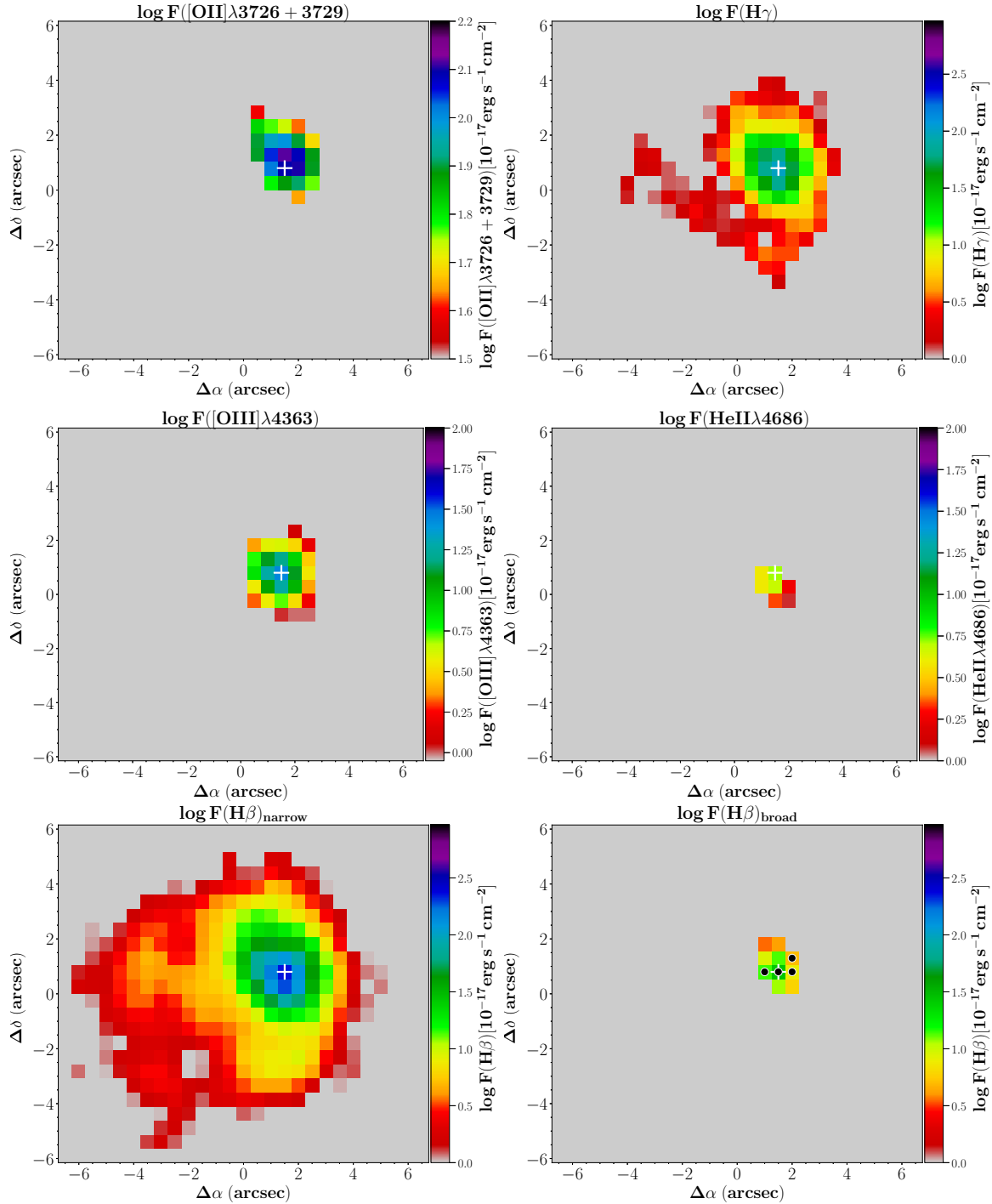**Figure 2.** Flux maps in logarithmic scale. Only fluxes with S/N > 3 are shown. East is left and North is up. The plus (+) sign indicating the Hα emission peak is plotted for orientation. The spaxels with no measurements available are left grey. The spaxels where we detect a P Cygni-like profile in the Hβ line are indicated with a black circle on the map for the Hβ broad emission.

4.2 Nebular physical-chemical properties on a spaxel-by-spaxel basis

We have used the expressions from Pérez-Montero (2017) to compute the physical properties and ionic abundances of the PHL 293B ionized gaseous nebulae. These expressions are derived from the PyNEB tool (Luridiana, Morisset & Shaw 2015).

In Fig. 7 we show the maps for the [OII]$\lambda3729$/$\lambda3726$ and [SII]$\lambda6717$/$\lambda6731$ line ratios which are good indicators of the average electron density (n_e) in a nebula (Osterbrock & Ferland 2006). For most of the spectra, the observed [OII] ([SII]) line ratios correspond to n_e values $\lesssim 300$ cm^{-3} ($\lesssim 100$ cm^{-3}), indicating a relatively low-density ionized gas in the central parts of PHL 293B.

For the [OIII]$\lambda4363$-emitting spaxels, we have computed the electron temperature T_e[OIII] values from the reddening corrected [OIII]$\lambda4363$/[OIII]$\lambda5007$ line ratio. We have measured the weak
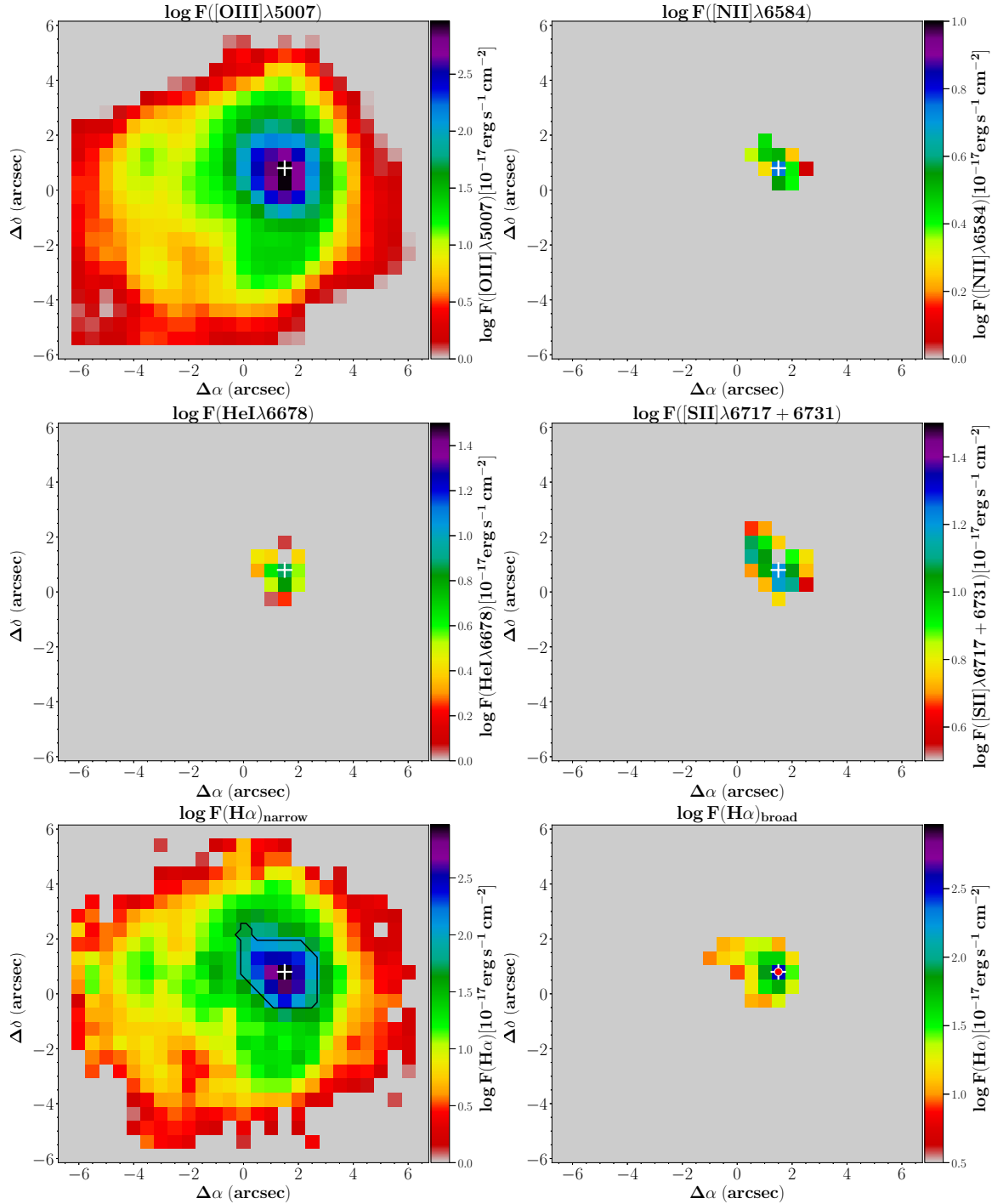
Figure 2. (continue). The spaxel where we detect a P Cygni-like profile in the Hα line is indicated with a red circle on the Hα broad emission map; this spaxel corresponds to the Hα emission peak. The black continuous line in the Hα narrow emission map demarcates the brightest area of the galaxy enclosing only spaxels with Hα S/N (per pixel) > 100 (see Section 5 for details).

[OIII]λ4363 line above 3σ for 29 spaxels which extend to an area of around 9.6 arcsec^2 equivalent to 0.12 kpc^2 (see Fig. 2). The top-left panel of Fig. 8 presents the map of the T_e[OIII] which reveales values going from $\gtrsim$ 14,000 K to near 20,000 K, with a good fraction of the points clustering around the average T_e value of $\sim$ 18,300 K. The relation between T_e[OIII] and the S/N measured for the [OIII]λ4363 line is plotted in the bottom panel of Fig. 8 where no systematic effects are observed. This is an evidence that

the largest values of T_e[OIII] that we derive are not an effect of overestimated [OIII]λ4363 flux measurements. We have used the T_e[OII]-T_e[OIII] empirical relationtionship from Pilyugin et al. (2006) to determine the T_e[OII] values since no low-excitation auroral line (e.g., [NII]λ5755) has been detected in any spaxel.

The O$^+$/H$^+$ and O^{2+}/H$^+$ ionic abundance ratios, were computed from the [OII]λ3726,29 and [OIII]λ5007 lines, respectively using the corresponding electron temperatures. A tiny fraction of
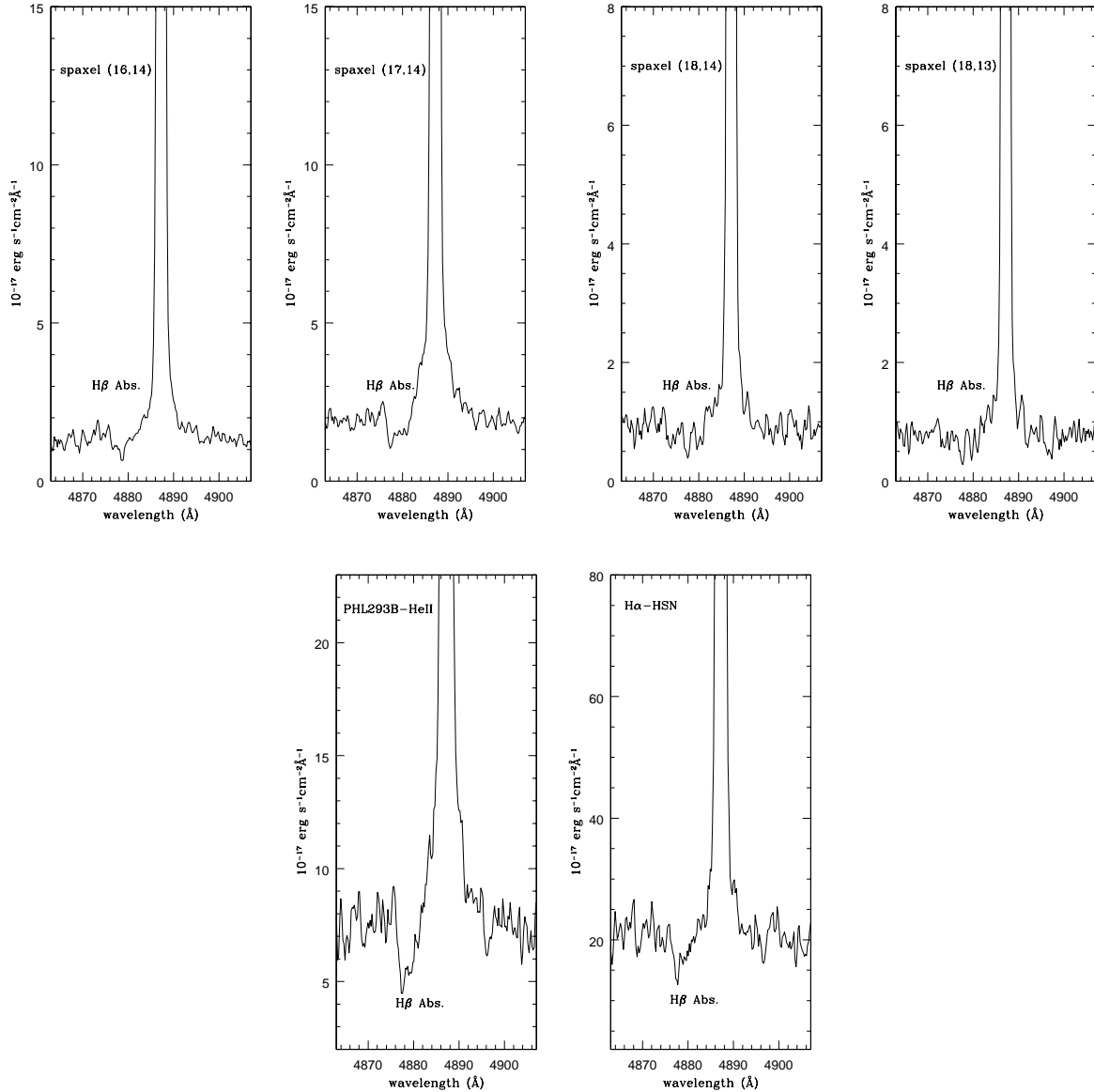
Figure 3. Spectral regions around Hβ where we detect P Cygni-like profiles. The *y-axis* shows the flux in units of 10^{-17} erg s^{-1} cm^{-2} Å^{-1}. *Top row*: the four individual spaxels marked with a black circle on the Hβ broad emission map (see Fig. 2); for each spaxel we show in parenthesis the corresponding cartesian coordinate (x,y) relative to the bottom left spaxel (0,0) in the maps. *Bottom row*: The spectra of the regions PHL 293B-HeII and Hα-HSN; the former is obtained by integrating the emission from all HeIIλ4686-emitting spaxels, while the latter corresponds to the sum of all spaxels with Hα S/N > 100 (see Section 5 for details on the integrated spectra).

the unseen O^{3+} ion is expected to be present in high-ionizing SF regions as the ones showing HeII emission. Based on the photoionization models from Izotov et al. (2006a), the O^{3+}/O ratio is > 1% only in the highest-excitation HII regions whose O^+/(O^+ + O^{2+}) is lower than 10%. We have checked that for all [OIII]λ4363-emitting spaxels (including non-HeIIλ4686 and HeIIλ4686 emitting spaxels), O^+/(O^+ + O^{2+}) is ≳ 10%; therefore the total O/H is assumed to be O^+/H^+ + O^{2+}/H^+. The spatial distribution of the derived 12+log(O/H) is displayed in the top-right panel of Fig. 8 with most of the spaxels (80%) showing oxygen abundance in the range of ≈ 7.5–7.6. Our results, thus, indicate that the warm gas-phase O/H in PHL 293B stands largely constant beyond hundreds of parsecs. This agrees with the absence of signif-

icant abundance gradient commonly observed in the ionized gas of HII galaxies (e.g., Kobulnicky & Skillman 1996; Izotov, et al. 1999; Thuan, Izotov & Foltz 1999; Izotov, Chaffee & Green 2001; Izotov, et al. 2004, 2006b; Papaderos, et al. 2006; Kehrig et al. 2008, 2013; Kehrig, et al. 2016; Pérez-Montero et al. 2009, 2011).

5 INTEGRATED SPECTRA ACROSS THE MEGARA FOV OF PHL 293B

Based on our IFU data we integrated individual spectra of selected galaxy regions. We created for the first time the integrated spectrum of PHL 293B by adding the flux in all the spaxels with Hα S/N (per

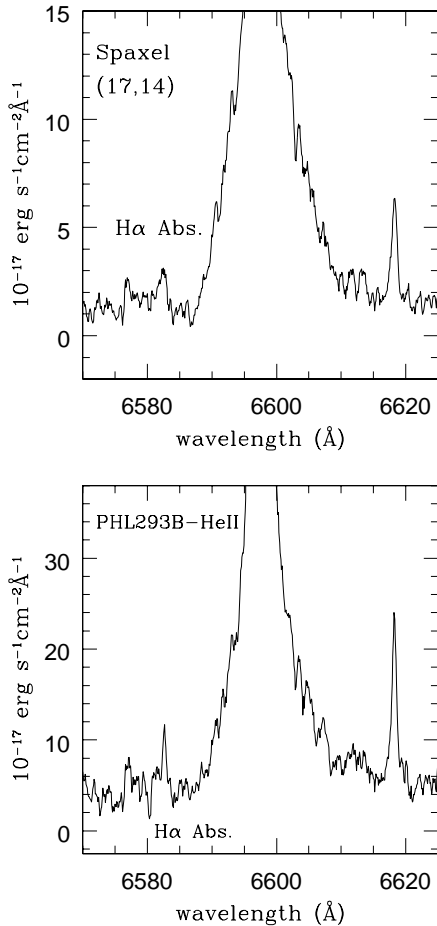**Figure 4.** Spectral regions around Hα showing hints for P Cygni-like profiles. The *y-axis* shows the flux in units of 10^{-17} erg s^{-1} cm^{-2} Å^{-1}. *Top panel*: spaxel (17,14) which corresponds to the Hα peak marked with a plus (+) sign on all maps; *Bottom panel*: Spectrum of the PHL 293B-HeII region as defined in the caption of Fig. 3 and in Section 5.
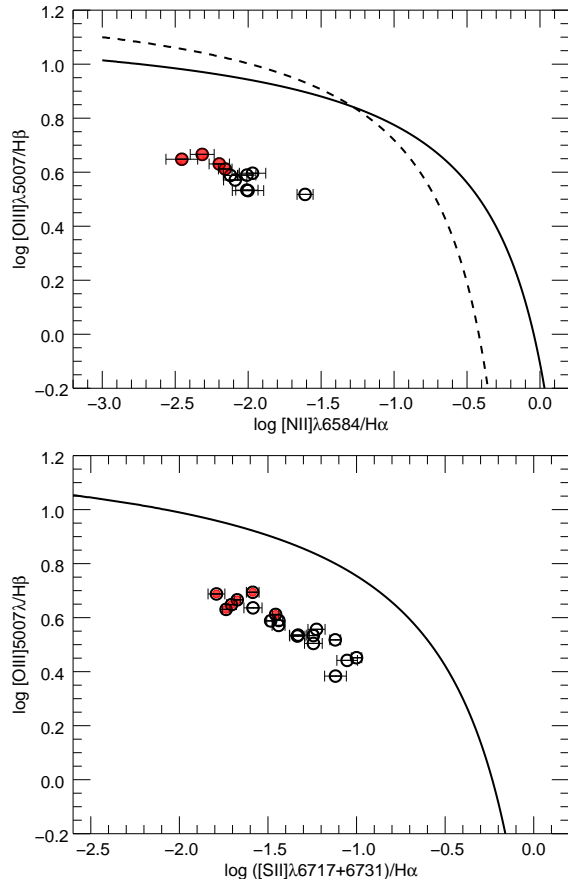

Figure 5. BPT diagnostic diagrams for PHL 293B. Open circles mark the individual spaxels from the data cube; red circles show the individual HeII-emitting spaxels. The solid line (in the two panels) indicates the theoretical demarcation limit from Kewley et al. (2001) that separates objects where the gas ionization is mainly due to hot massive stars (below and to the left of the curve) from those where other ionizing mechanism is required. The dashed line in the [NII]λ6584/Hα plot (top panel) depicts the boundary between SF systems and AGNs from Kauffmann et al. (2003). Error bars in the *y-axis* are the same size or smaller than the symbols, and are not plotted for the sake of clarity.

spaxel) > 3; this matches an area of ∼ 194 arcsec^2 (∼ 2.4 kpc^2) enclosing basically all the nebular emission across our FOV. In addition, by summing the emission from the spaxels with Hα S/N > 100 (∼ 11.5 arcsec^2), we simulate the spectrum of the brightest region of the galaxy (hereafter Hα-HSN region[4]), and whose boundary is shown overplotted on the map of Hα (see Fig. 2). Finally, we obtained the spectrum of the region that we name PHL 293B-HeII. To do so we have integrated all HeII-emitting spaxels which covers ∼ 3.5 arcsec^2 (see the HeII map in Fig. 2).

The 1D spectra mentioned above are presented in Fig. 9. We derive the fluxes of the emission-lines and associated uncertainties for these spectra using the same method as for individual spaxels (see Section 3). We computed the logarithmic reddening coefficient, C(Hβ), by performing a least square fit to the ratio of the measured-to-theoretical Balmer decrements as a function of the Miller & Mathews (1972) galactic reddening law (see also Hägele, et al. 2008). The uncertainty of the fit is adopted as the error in C(Hβ). The narrow component of the four strongest Balmer emission lines (Hα, Hβ, Hγ, Hδ) have been used. Intrinsic Balmer

line ratios were taken from Osterbrock & Ferland (2006) assuming case B recombination with electron temperature T$_e$=2×10^{4}K: (Hδ/Hβ)$_{theo}$=0.26, (Hγ/Hβ)$_{theo}$=0.47, (Hα/Hβ)$_{theo}$=2.75. Some issues were found concernig the C(Hβ) computation. The blue grating covers the Hδ and Hγ, and the green spectra include both Hγ and Hβ, while Hα is measured in the red grating (see Section 2). We match the blue and green spectra by using the Hγ line as reference which is measurable in both. We could not connect the green and red spectra since they share no lines. Thus, to minimize errors in the de-reddened ratios between a certain emission line and Hβ, we always take first its ratio in relation to the closest hydrogen emission line (i.e. Hδ in the case of [OII]λ3726, [OII]λ3729 and [NeIII]3868λ; Hα in the case of [NII], HeI6678 and [SII]) and then we renormalize it using the corresponding theoretical Balmer ratio (e.g., Pérez-Montero et al. 2009, 2011; Kehrig et al. 2011).

Table 2 presents the relative fluxes of the de-reddened narrow emission lines measured from the integrated spectra; fluxes are normalized to the Hβ flux = 1000. We note that the values of C(Hβ) obtained here are in agreement with values derived for PHL 293B in the past (e.g., Izotov, Thuan, & Guseva 2012; Terlevich et al.

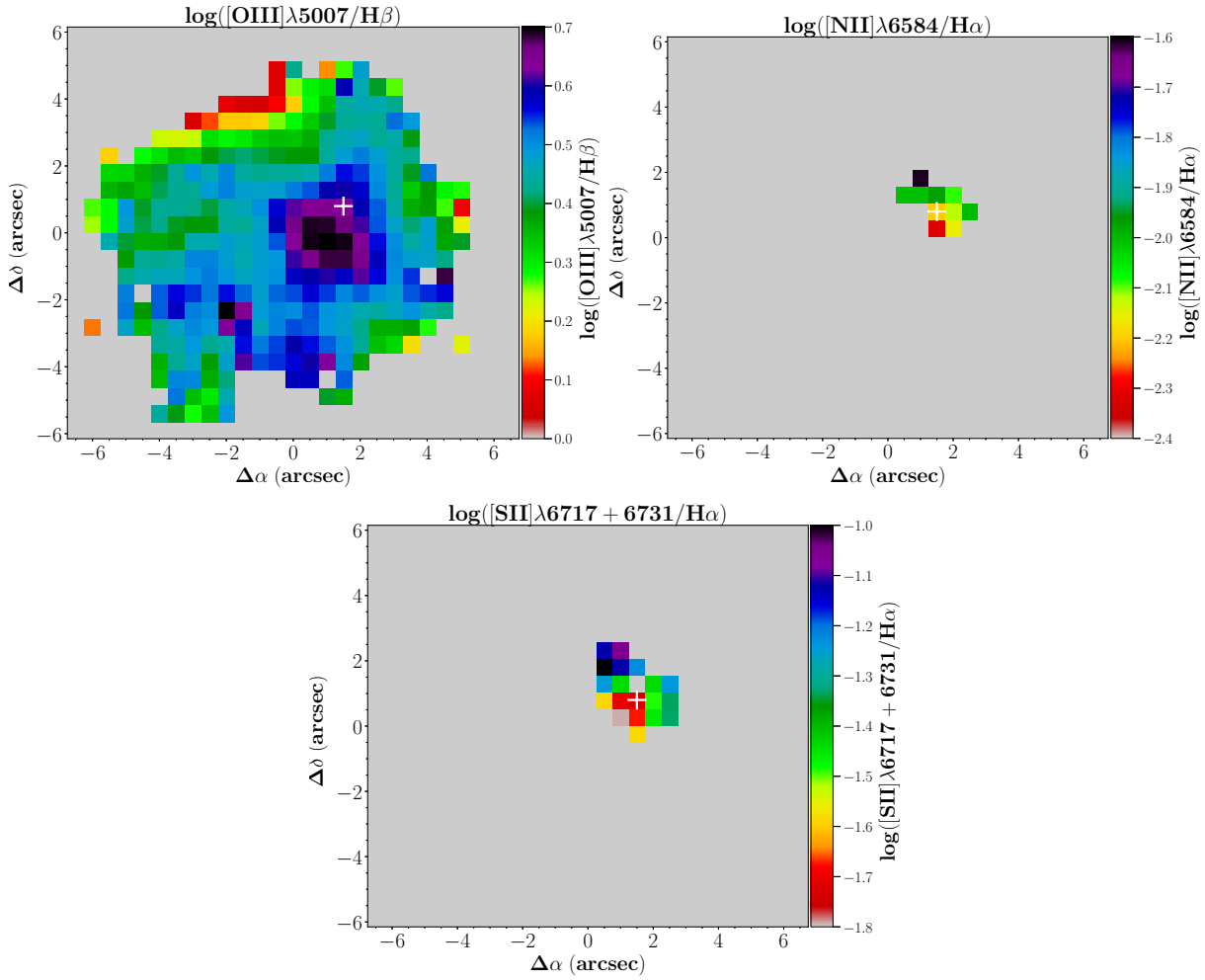[4] HSN from High Signal to Noise ratio.

Figure 6. Maps of line ratios in logarithmic scale. East is left and North is up. The plus (+) sign is as indicated in
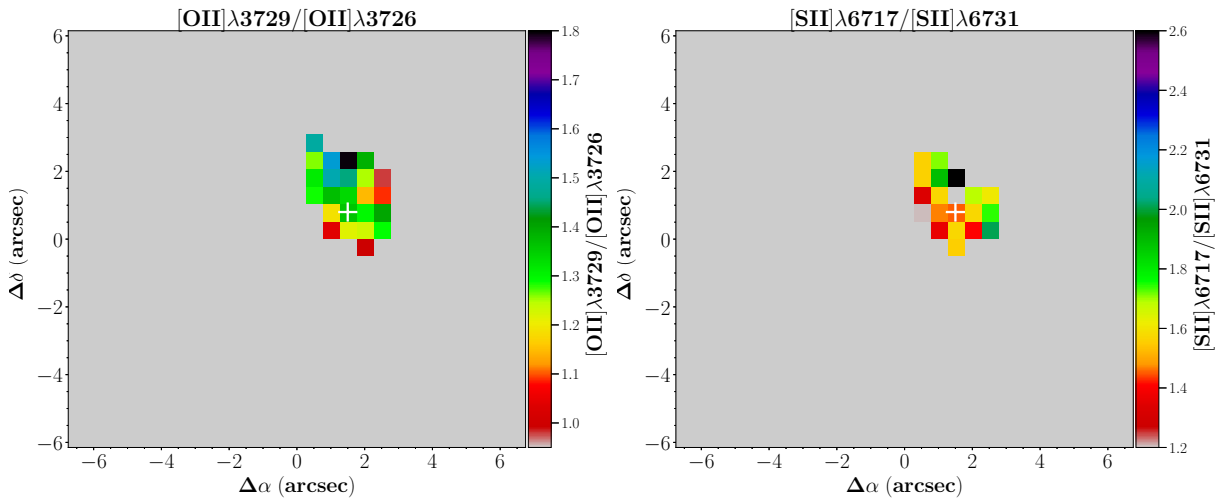
Fig. 2.

Figure 7. Indicators of nebula electron density. Maps for [OII]λ3729/[OII]λ3726 and [SII]λ6716/[SII]λ6731. East is left and North is up. The plus (+) sign is as indicated in
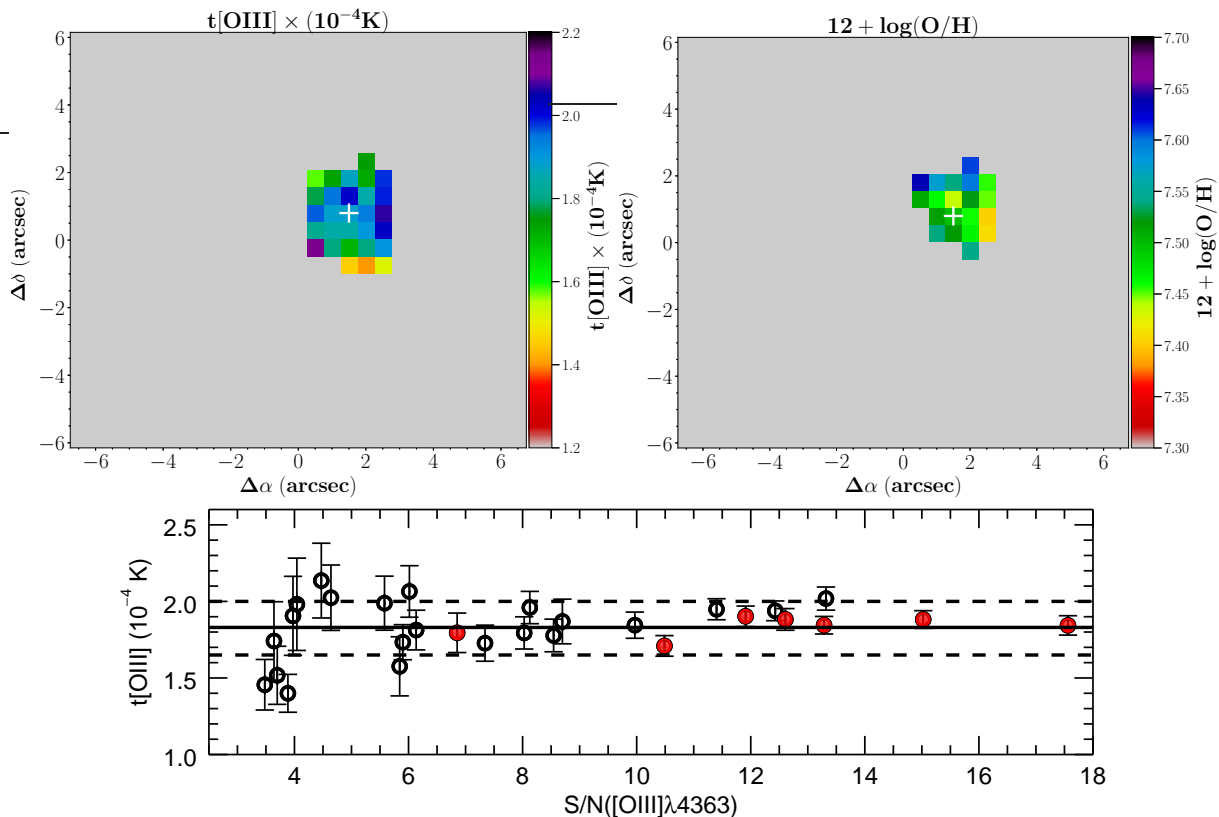
Fig. 2.

Figure 8. *Top-left panel*: Map of the [OIII]λ4363-derived T_e[OIII]. *Top-right panel*: Map of oxygen abundance derived only for spaxels with T_e[OIII] measurements available. The plus (+) sign is as indicated in Fig. 2. *Bottom panel*: T_e[OIII] versus the S/N of the [OIII]λ4363 line flux. Open circles represent individual spaxels; red circles indicate the seven HeIIλ4686-emitting spaxels; the solid horizontal line marks the mean value for T_e[OIII] ~ 1.83×10^4 K, while dotted lines represent ± 1σ.

2014). Also, the listed Hα/Hβ and Hδ/Hβ ratios acceptably match their theoretical recombination values; the Hγ/Hβ ratio shown in Table 2 makes use of the green-Hγ flux, and is about 10%-15% smaller than the theoretical one. We verify that using the blue-Hγ flux instead, the ratio between the de-reddened and theoretical Hγ/Hβ lowers down to 3%-5%. The line ratios uncertainties consider error flux measurements and the error in C(Hβ), but do not take systematic uncertainties, e.g., due to the blue-green match. We note that the effects of these uncertainties on the line ratios upon which oxygen abundance and T_e[OIII] estimates are based should be marginal since we obtain values in accord with other authors (see below). Since the [OII] lines are the most affected by extinction in our spectra, as a further check, we also corrected for reddening [OII]λλ3726,3729/Hβ using only the green-Hγ-to-Hβ ratio. We found that the variations in [OII]λλ3726,3729/Hβ are within the quoted uncertainties in Table 2.

For our three selected galaxy regions (PHL 293B integrated, PHL 293B-HeII, Hα-HSN), we calculated physical properties and oxygen abundances as explained in Section 4 for single spaxel spectra. We calculated the nitrogen ionic abundance ratio, N^+/H^+, from the PYNEB-based expression from (Pérez-Montero 2017), using the [NII]λ6584 emission line and assuming Te[NII] ≈ Te[OII]; we derived the N/O ratio under the premise that N/O=N^+/O^+, based on the similitude of the ionization potentials of the ions N^+ and O^+. Table 2 also lists the values of C(Hβ) and physical-chemical properties obtained for each spectrum region.

By looking at Table 2 and Fig. 5, we find that the measurements of the integrated line-ratios [OIII]λ5007/Hβ, [NII]λ6584/Hα,

[SII]λ6717,6731/Hα for the three selected regions are located below the demarcation lines in the BPT diagrams which implies an HII region-like ionization.

The comparison among the integrated electron temperature values from Table 2 shows similar T_e[OIII], considering the uncertainties. Concerning the oxygen abundances, we also find that the spectra of the regions PHL 293B-HeII, Hα-HSN, and PHL 293B-integrated yield equivalent values within the corresponding error bars. This is telling us that the metallicity obtained from the PHL 293B-integrated spectrum matches the O/H from the other two (physically smaller) selected zones. Therefore, according to our MEGARA data, the gas metallicity of PHL 293B is not only spatially homogenous (see previous section), but also independent of the aperture applied. Here, we take the O/H abundance of the integrated-spectrum [12+log (O/H)=7.64 ± 0.06 ~ 8% solar metallicity] as the representative metallicity of PHL 293B. This value is consistent, within the errors, with those reported in previous work (e.g., Kinman & Davidson 1981; Izotov, Thuan & Guseva 2007; Papaderos et al. 2008; Guseva, et al. 2009).

Regarding the nitrogen abundance, we find that the Hα-HSN and PHL 293B-HeII regions present similar N/O ratios within the uncertainties (see Table 2). The N/O values derived here are in agreement with the typical value of Log(N/O) ≈ -1.5 to -1.6 characteristic for the plateau in the 12+Log(O/H) vs. Log(N/O) relation observed for low-metallicity systems (e.g., Garnett 1990; Thuan, Izotov & Lipovetsky 1995; Izotov & Thuan 1999; van Zee & Haynes 2006; Mollá et al. 2006; Pérez-Montero et al. 2011). Moreover, we confirm that the N/O ratios for these two re-

gions match those obtained in earlier studies of PHL 293B (e.g., French 1980; Izotov, Thuan & Guseva 2007).

In Table 3 we list the observed fluxes and dispersion of the broad and narrow emission components of Hα and Hβ lines for the three integrated spectra described in this section. The origin of the broad emission and P Cygni-like features in the Balmer lines seen in the spectra of PHL 293B has been debated for many years. Discrepant scenarios involving a luminous blue variable star eruption, an expanding supershell or a stationary wind driven by a young cluster wind, and strongly-radiative stationary cluster wind have been proposed (e.g., Izotov & Thuan 2009; Terlevich et al. 2014; Tenorio-Tagle, et al. 2015). Burke, et al. (2020) review the previous interpretations for the nature of PHL 293B including new 2019 Gemini data, and find a recent fading of broad Hα emission (see also Allan et al. 2020); a broad to narrow Hα flux ratio (Hα B/N) of 0.41 from 2001 SDSS data and 0.10 from 2019 Gemini data are reported by Burke, et al. (2020). Here we find Hα B/N $\sim$ 0.10 for all the three integrated regions indicating that the dissipation of the broad Hα emission might have begun in 2017 when our observations were performed (see Table 3). However, while our data reveal P Cygni-like features in Hβ and Hα (see Figs. 3 and 4), P Cygni profile in Hα is not visible in the 2019 Gemini spectra according to Burke, et al. (2020)[5]. A long-lived Type IIn supernova (SN IIn) is proposed to be the most likely explanation for the optical and spectral variability of PHL 293B by Burke, et al. (2020). However, the lack of X-rays ($\lesssim 3 \times 10^{38}$ erg s^{-1}; e.g., Prestwich, et al. 2013; Terlevich et al. 2014) in PHL 293B remains the big challenge to the SN IIn scenario. Larger timescales spectroscopic follow-up should be necessary to clarify the variable spectral features of PHL 293B, but this is outside the scope of our study.

6   THE NEBULAR HEIIλ4686 IN PHL 293B

Photons with energy beyond 54 eV are needed to ionize He twice, so HeII-emitting objects should host a relatively hard radiation field. While nebular HeII emitters are atypical of nearby galaxies, they are expected to be usual at high-z (z $\gtrsim$ 6) due to the predicted harder UV-ionizing spectra at the lower metallicities typical in the far-away Universe (e.g., Smith, et al. 2015; Stark 2016; Stanway & Eldridge 2019). Next generation telescopes (e.g., JWST, ELT) are expected to detect the rest-frame UV of thousands of high-ionizing galaxies in the reionization era. Therefore, studying the HeII-ionization in metal-poor local objects is crucial to illuminate the properties of these reionization-epoch systems.

It is to be noted that the fraction of HeII-emitting systems among metal-poor objects tend to be larger than that for higher metallicity galaxies observed in the local Universe (e.g., Kehrig et al. 2011; Shirazi & Brinchmann 2012). Ultra luminous X-ray binaries (ULXB), hot massive stars and shocks are among the leading candidate sources discussed in the literature to explain the nebular HeII excitation in nearby SF galaxies (e.g., Garnett, et al. 1991; Kehrig et al. 2011; Shirazi & Brinchmann 2012; Szécsi, et al. 2015; Senchyna, et al. 2020). However, despite observational and theoretical efforts, the origin of the He$^+$ ionization is far to be a settled matter in several cases (e.g., Garnett, et al. 1991; Kehrig et al. 2015; Kehrig, et al. 2018; Plat, et al. 2019; Kubátová, et al. 2019; Zackrisson & Vikaeus 2020). Current stellar models keep failing to reproduce the total emergent flux beyond

54 eV, specially in metal-poor galaxies (e.g., Kehrig et al. 2015; Kehrig, et al. 2018; Stanway & Eldridge 2019).

The existence of narrow HeIIλ4686 emission in PHL 293B has been noted before from long-slit spectroscopy (e.g., Izotov, Thuan & Guseva 2007; Papaderos et al. 2008; Guseva, et al. 2009; Izotov et al. 2011). Here, we produce the first HeIIλ4686 spectral map of PHL 293B using MEGARA (see Fig. 2). From our data, we checked that the FWHM of the HeIIλ4686 line matches that of other nebular emission lines like the strong [OIII]λ5007. The measured values of the mean and standard deviation for the FWHM(HeII)/FWHM([OIII]λ5007) ratio are $\sim$ 1.10 and 0.10, respectively. The narrow line profile for the HeIIλ4686 emission and its spatial extent are evidence of its nebular origin (see also Shirazi & Brinchmann 2012).

PHL 293B was observed with the *Chandra X-ray Observatory* on 2009 September for a total exposure time of 7.7 ks using the ACIS-S3 detector. There is no detection of X-ray emission up to an upper limit of $\sim 3 \times 10^{38}$ erg s^{-1} (Prestwich, et al. 2013; Terlevich et al. 2014). This indicates that X-ray sources are unlikely to be the main responsible for the He II ionization in PHL 293B. On the other hand, the BPT line-ratios measured both from the single HeII-emitting spaxels and integrated spectra show values typical of HII region-like ionization (see Fig. 5 and Table 2) indicating hot massive stars as the dominant excitation source. This agrees with Burke, et al. (2020) who claim that the narrow emission gas in PHL 293B is likely the HII region ionized primarily by stellar emission. Wolf-Rayet (WR) emission bumps are not detected in the spectra of PHL 293B. This means that different types of hot stars other than WRs should be contributing to the HeII excitation. This result agrees with the studies of the HeII-emitting extremely metal-poor (XMP) galaxies IZw18 and SBS 0335-052E (see Kehrig et al. 2015; Kehrig, et al. 2018). A detailed comparison of our observations to model predictions would be needed to constrain the hot ionizing stellar population in PHL 293B, but this exercise is beyond the scope of this paper.

For the PHL 293B-HeII spectrum (obtained by adding all the HeII-emitting spaxels; see Fig. 2 and Section 5), we computed the HeII ionizing photon flux, Q(HeII)$_{PHL\ 293B-HeII}$ = 3.66$\times 10^{49}$ photons s^{-1} (see Table 2), from the corresponding reddening-corrected luminosity L(HeII) using the relation Q(HeII)=L(HeII)/[j(λ4686)/α_B(HeII)] (assuming case B recombination, and T_e([OIII]=2$\times 10^4$ K; Osterbrock & Ferland 2006). Applying the same method for the Hα-HSN region, whose area includes the PHL 293B-HeII region (see Fig. 2 and Section 5 for details) we find that the Hα-HSN region produces Q(HeII)= 4.16$\times 10^{49}$ photon s^{-1} (see Table 2). This is $\sim$ 14 % higher than Q(HeII)$_{PHL\ 293B-HeII}$ which indicates that some small fraction of gas beyond the PHL 293B-HeII region is also emitting He$^+$-ionizing photons. The PHL 293B-HeII and Hα-HSN regions, together produce a total Q(HeII) = 7.82 $\times 10^{49}$ photons s^{-1} which can be taken as the HeII ionizing budget measured for PHL 293B. It is worth noticing that the PHL 293B-integrated spectrum, created by summing almost all the emission across the MEGARA FOV, does not show the HeII line (see Table 2). In this regard one should bear in mind that searches for reionization-era HeII-emitters, for which only the total integrated spectra will be available, might be biased in the sence shown here,i.e., that a non-detection of the HeII line does not necessarily mean the intrinsic absence of HeII emission.

Using integral field spectroscopy (IFS), we also studied the spatial distribution of the nebular HeII emission for the XMPs SBS 0335-052E and IZw18 (Kehrig et al. 2015; Kehrig, et al. 2016, 2018). When comparing the observed Q(HeII) for different regions

---

[5] Gemini spectra from Burke, et al. (2020) cover from 5500 - 7500 Å.

Table 2. De-reddened narrow emission line-fluxes relative to Hβ=1000 and physical properties from three selected regions[a]

Wavelength (Å)	Selected regions		
	PHL 293B-Integrated[b]	Hα-HSN[c]	PHL 293B-HeII[d]
3726 [O II]	585 ± 168	464 ± 46	296 ± 32
3729 [O II]	760 ± 118	544 ± 42	340 ± 27
3868 [NeIII]	417 ± 30	418 ± 7	407 ± 6
4100 Hδ	286 ± 16	277 ± 5	271 ± 4
4340 Hγ	390 ± 18	417 ± 10	412 ± 9
4363 [O III]	84 ± 14	106 ± 6	113 ± 5
4686 He II	—	20 ± 2	26 ± 2
4714 [Ar IV]	—	21 ± 2	24 ± 3
4740 [Ar IV]	—	14 ± 2	16 ± 2
5007 [O III]	3568 ± 38	4068 ± 44	4406 ± 32
6563 Hα (Narrow)	2717 ± 55	2831 ± 39	2804 ± 28
6584 [N II]	—	20 ± 3	16 ± 4
6678 HeI	—	24 ± 1	23 ± 1
6717 [S II]	82 ± 10	54 ± 2	36 ± 1
6731 [S II]	—	36 ± 2	27 ± 2
c(Hβ)	0.11 ± 0.02	0.14 ± 0.01	0.30 ± 0.01
F(Hβ) (erg s^{-1} cm^{-2})	4.28×10^{-14}	2.74×10^{-14}	1.86×10^{-14}
F(HeII) (erg s^{-1} cm^{-2})	—	5.41×10^{-16}	4.76×10^{-16}
L(HeII)(erg s^{-1})[e]	—	3.45×10^{37}	3.04×10^{37}
Q(HeII)(photon s^{-1})[f]	—	4.16×10^{49}	3.66×10^{49}
log ([N II]6584/Hα)	—	-2.16	-2.25
log ([S II]6717+6731/Hα)	—	-1.50	-1.66
log ([O III]5007/Hβ)	0.55	0.61	0.64
T_e([O III]) (K)	16,335 ± 1500	17,243 ± 548	17,089 ± 450
T_e([O II])[g] (K)	14,361 ± 1080	15,015 ± 394	14,904 ± 324
12+log(O^+/H^+)	7.08 ± 0.11	6.90 ± 0.04	6.71 ± 0.04
12+log(O^{++}/H^+)	7.50 ± 0.07	7.51 ± 0.02	7.55 ± 0.02
12+log(O/H)[h]	7.64 ± 0.06	7.60 ± 0.02	7.61 ± 0.02
12+log(N^+/H^+)	—	5.21 ± 0.07	5.12 ± 0.11
log(N/O)	—	-1.68 ± 0.08	-1.59 ± 0.11

(a) In all cases, the reddening correction for each line flux was performed relative to the closest Balmer recombination line (see text for details)
(b) PHL 293B-integrated spectrum obtained by co-adding all spaxels with Hα S/N > 3
(c) Spectrum created by adding all spaxels with Hα S/N > 100
(d) Spectrum obtained by summing all HeII-emitting spaxels
(e) HeII luminosity at the distance of 23.1 Mpc
(f) Number of ionizing photons shortward of the He$^+$ edge (see the text for details)
(g) T_e[OII] = 0.72 × T_e[OIII] + 0.26 (Pilyugin et al. 2006)
(h) O/H = O$^+$/H$^+$ + O^{2+}/H$^+$

Table 3. Fit parameters of the broad and narrow hydrogen (Hβ, Hα) emission lines for the regions listed in Table2

Region[a]	Property	Hβ Narrow	Hβ Broad	Hα Narrow	Hα Broad
	Flux[b]	3296 ± 32	—	9720 ± 61	1005 ± 79
PHL 293B-Integrated	σ_{obs} (Å)[c]	0.50	—	0.46	2.3
	σ_{obs} (Km/s)[d]	31	—	21	105
	Flux[b]	1978 ± 16	103 ± 21	6203 ± 15	589 ± 31
Hα-HSN	σ_{obs} (Å)[c]	0.49	2.22	0.46	3.17
	σ_{obs} (Km/s)[d]	30	137	21	145
	Flux[b]	933 ± 5	65 ± 9	3247 ± 7	375 ± 19
PHL 293B-HeII	σ_{obs} (Å)[c]	0.50	2	0.46	3.8
	σ_{obs} (Km/s)[d]	31	123	21	174

(a) Regions as defined in Table 2.
(b) Observed fluxes in units of 10^{-17} erg s^{-1} cm^{-2}.
(c) and (d) Observed σ (= FWHM/2.35) in units of Angstrom and Km/s, respectively

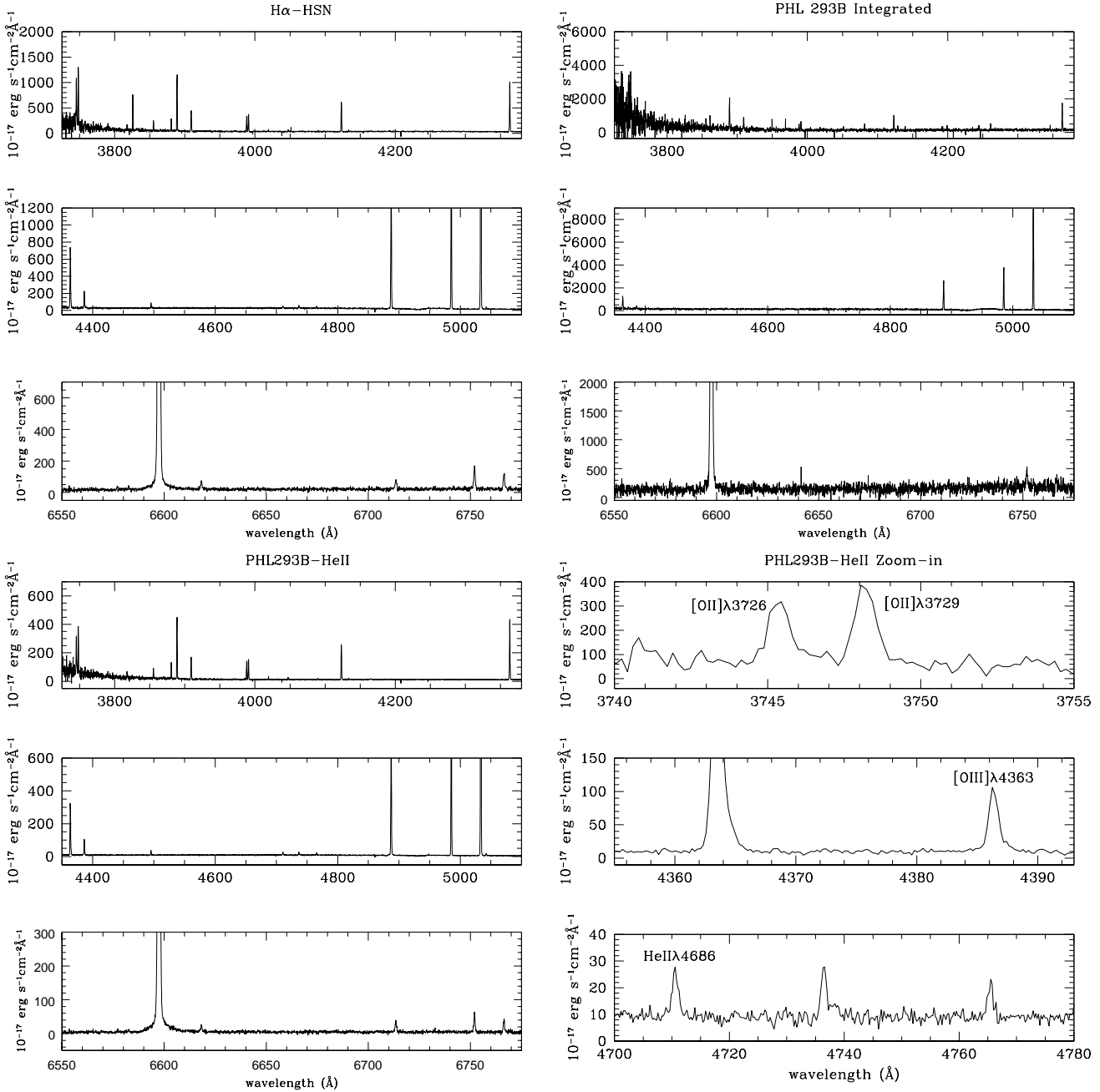**Figure 9.** Flux-calibrated spectra of the three regions defined in Section 5. The *y-axis* shows the flux in units of 10^{-17} erg s^{-1} cm^{-2} Å^{-1}. *Left column, three first rows from top to bottom:* the VPH405-LR, VPH480-LR, and VPH665-HR spectra for the Hα-HSN region. *Right column, three first rows from top to bottom:* the VPH405-LR, VPH480-LR, and VPH665-HR spectra for the PHL 293B-integrated region. *Left column, the three last rows from top to bottom:* the VPH405-LR, VPH480-LR, and VPH665-HR spectra for the PHL 293B-HeII region. For illustrative purposes, in the case of the PHL 293B-HeII spectrum, the *last three rows of the right column* display a zoomed-in view of the [OII] doublet, and of the wavelength ranges $\sim$ 4355-4390 Å and $\sim$ 4700-4780 Å showing the [OIII]λ4363 and nebular HeIIλ4686 lines, respectively

across SBS 0335-052E and IZw18, we find, for both objects, that the highest absolute HeII flux and maximum Q(HeII) values correspond to the integrated spectrum of the galaxy, contrary to what we see in PHL 293B. This could suggest that the fraction of HeII-ionizing hot stars, with respect to the total massive stellar content, should be higher in SBS 0335-052E and IZw18 in comparison to the that of PHL 293B, and that a higher amount of He$^+$-ionizing photons is reaching larger distances from the central star clusters in both SBS 0335-052E and IZw18. This might be related to the fact

that, although the three objects are very low-Z, the specific star formation rate (sSFR) of SBS 0335-052E and IZw18 (170 Gyr^{-1} and 166 Gyr^{-1}, respectively; Schneider, Hunt & Valiante 2016) is > 20 times that of PHL 293B sSFR $\sim$ 6 Gyr^{-1} (Filho, et al. 2013). Of course, higher statistics is necessary to make stronger statements on which properties can be dominant factors to determine the HeII emitting nature of a galaxy.

All the results described above testify the importance of IFS

for this kind of analysis, which allows us to collect all HeII emission, and therefore deriving the absolute HeII ionization budget.

7 SUMMARY AND CONCLUSIONS

We have analysed MEGARA observations of the nearby, very metal-deficient galaxy PHL 293B. This kind of objects constitute excellent laboratories for probing the conditions of galaxies in the early universe. The data cover the optical wavelength range ($\sim$ 3700-6800 Å) within a field-of-view of $\sim 12.5 \times 11.3$ arcsec^2. MEGARA-IFU scans the entire spatial extent of the PHL 293B main body providing us with a new 2D view of the ionized ISM in this galaxy. Maps for the spatial distribution of relevant emission lines, line-ratios and physical-chemical properties for the ionized gas have been discussed. We were able to detect low intensity broad components and P Cygni-like profiles in the Balmer lines in agreement with previous work. We have checked that such components coincide spatially with the brightest star-forming cluster of the galaxy.

The BPT-line ratios ([OIII]λ5007/Hβ, [NII]λ6584/Hα, [SII]$\lambda\lambda$6717,6731/Hα) measured both from individual spaxels and integrated spectrum regions agree with HII-like ionization. We measured the [OIII]λ4363 line flux over the central parts of the galaxy covering an area of $\sim$ 0.12 kpc^2. For this zone, we measured O/H directly from the derived electron temperature T$_e$[OIII], and we find no significant variations in oxygen abundance; most of spaxels have 12+log(O/H) values spanning around $\approx$ 7.5–7.6. For the first time, we derive the PHL 293B integrated spectrum by summing the spaxels with Hα S/N > 3. We take the O/H abundance of the PHL 293B integrated spectrum, 12+log (O/H)=7.64 $\pm$ 0.06 $\sim$ 8% solar metallicity, as the representative metallicity of the galaxy. Such value concurs with the ones on a spaxel-by-spaxel basis, and it also matches with those found in the literature.

Here, we derive the first spectral map for the nebular HeIIλ4686 line and compute the HeII ionization budget in PHL 293B. Our observations together with data from the literature indicate that neither Wolf-Rayet stars nor X-ray binaries are the main responsible for the HeII ionization in PHL 293B. This is in the line of our studies on the two XMPs SBS 0335-052E and IZw18 based on IFS. Additional IFS studies of large samples of very metal-deficient and nebular HeII-emitters are needed to better understand the nature of these objects.

REFERENCES

Allan A., et al., 2020, arXiv:2003.02242
Asplund M., et al., 2009, ARA&A, 47, 481
Baldwin J. A., Phillips M. M., Terlevich R., 1981, PASP, 93, 5
Burke C. J., et al., 2020, arXiv:2002.12369
Cairós L. M., et al., 2001, ApJS, 136, 393
Cairós L. M., et al., 2009, A&A, 507, 1291
Cairós L. M., et al., 2010, A&A, 520, A90
Carrasco E. et al., 2018, Proceedings of the SPIE, Volume 10702, p.1070216
Duarte Puertas S., et al., 2019, A&A, 629, A102
Fernández V., et al., 2018, MNRAS, 478, 5301
Filho M. E., et al., 2013, A&A, 558, A18
French H. B., 1980, ApJ, 240, 41
Garnett D. R., 1990, ApJ, 363, 142
Garnett D. R., et al., 1991, ApJ, 373, 458
Gil de Paz A. et al., 2018, Proceedings of the SPIE, Volume 10702, p.1070217
Guseva N. G., et al., 2017, A&A, 599, A65
Guseva N. G., et al., 2009, A&A, 505, 63
Hägele G. F., et al., 2008, MNRAS, 383, 209
Izotov Y. I., Thuan T. X., 1999, ApJ, 511, 639
Izotov Y. I., et al., 1999, ApJ, 527, 757
Izotov Y. I., Chaffee F. H., Green R. F., 2001, ApJ, 562, 727
Izotov Y. I., et al., 2004, A&A, 421, 539
Izotov Y. I., et al., 2006a, A&A, 448, 955
Izotov Y. I., et al., 2006b, A&A, 459, 71
Izotov Y. I., Thuan T. X., Guseva N. G., 2007, ApJ, 671, 1297
Izotov Y. I., et al., 2011, A&A, 533, A25
Izotov Y. I., Thuan T. X., 2009, ApJ, 690, 1797
Izotov Y. I., Thuan T. X., Guseva N. G., 2012, A&A, 546, A122
Izotov Y. I., et al., 2018, MNRAS, 473, 1956
Izotov Y. I., Thuan T. X., Guseva N. G., 2019, MNRAS, 483, 5491
James B. L., et al., 2017, MNRAS, 465, 3977
Kauffmann G., et al., 2003, MNRAS, 346,1055
Kehrig C., Telles E., Cuisinier F., 2004, AJ, 128, 1141
Kehrig C., et al., 2006, A&A, 457, 477
Kehrig C., et al., 2008, A&A, 477, 813
Kehrig C.,Oey M. S., Crowther P. A. et al., 2011, A&A, 526, A128
Kehrig C., et al., 2013, MNRAS, 432, 2731
Kehrig C., et al., 2015, ApJ, 801, L28
Kehrig C., et al., 2016, MNRAS, 459, 2992
Kehrig C., et al., 2018, MNRAS, 480, 1081
Kewley L.J., et al., 2001, ApJ, 556, 121
Kobulnicky H. A., Skillman E. D., 1996, ApJ, 471, 211
Kinman T. D., Davidson K., 1981, ApJ, 243, 127
Kubátová B., et al., 2019, A&A, 623, A8
Lehnert M. D., van Driel W., Le Tiran L., Di Matteo P., Haywood M., 2015, A&A, 577, A112
López-Sanjuan C., et al., 2019, A&A, 631, A119

Luridiana V., Morisset C., Shaw R. A., 2015, A&A, 573, A42

Mainali R., et al., 2018, MNRAS, 479, 1180

Markwardt, C. B., 2009, Astronomical Data Analysis Software and Systems XVIII, 411, 251

Miller J. S., Mathews W. G., 1972, ApJ, 172, 593

Osterbrock D. E., Ferland G. J., 2006, Astrophysics of Gaseous Nebulae and Active Galactic Nuclei (CA: University Science Books)

Papaderos P., et al., 2006, A&A, 454, 119

Papaderos P., et al., 2008, A&A, 491, 113

Mollá M., et al., 2006, MNRAS, 372, 1069

Pascual S., et al., 2019, Highlights on Spanish Astrophysics X, Salamanca, Spain, p.227

Pérez-Montero E., et al., 2009, A&A, 497, 53

Pérez-Montero E., et al., 2011, A&A, 532, A141

Pérez-Montero E., 2017, PASP, 129, 043001

Pilyugin L. S., et al., 2006, MNRAS, 370, 1928

Plat A., et al., 2019, MNRAS, 490, 978

Prestwich A. H., et al., 2013, ApJ, 769, 92

Sánchez S. F., et al., 2012, A&A, 538, A8

Sánchez S. F., 2010, ARA&A, 58, annurev

Schneider R., Hunt L., Valiante R., 2016, MNRAS, 457, 1842

Schlafly E. F., Finkbeiner D. P., 2011, ApJ, 737, 103

Senchyna P., et al., 2019, MNRAS, 488, 3492

Senchyna P., et al., 2020, MNRAS, 494, 941

Shirazi M., Brinchmann J., 2012, MNRAS, 421, 1043

Smith A., et al., 2015, MNRAS, 449, 4336

Sobral D., et al., 2019, MNRAS, 482, 2422

Stanway E. R., Eldridge J. J., 2019, A&A, 621, A105

Stark D. P., 2016, ARA&A, 54, 761

Szécsi D., et al., 2015, A&A, 581, A15

Tenorio-Tagle G., et al., 2015, ApJ, 800, 131

Terlevich R., et al., 2014, MNRAS, 445, 1449

Thuan T. X., Izotov Y. I., Lipovetsky V. A., 1995, ApJ, 445, 108

Thuan T. X., Izotov Y. I., Foltz C. B., 1999, ApJ, 525, 105

Thuan T. X., Izotov Y. I., 2005, ApJS, 161, 240

Ucci G., et al., 2019, MNRAS, 483, 1295

van Zee L., Haynes M. P., 2006, ApJ, 636, 214

Westera P., et al., 2004, A&A, 423, 133

Yan R., et al., 2016, AJ, 151, 8

Zackrisson E., Vikaeus A., 2020, IAUS, 341, 187